Nanoscale

Single Nanomaterial Level Investigation of ZnO Nanorod Sulfidation Reaction via Position Resolved Confocal Raman Spectroscopy

Journal:	*Nanoscale*
Manuscript ID	NR-ART-07-2018-006039.R1
Article Type:	Paper
Date Submitted by the Author:	31-Oct-2018
Complete List of Authors:	Hansen, Matthew; Georgetown University Truong, Johnson; Georgetown University Szychowski, Brian; University of Maryland Baltimore County, Chemistry and Biochemistry Xie, Tian; Georgetown University, Department of Chemistry Daniel, Marie-Christine; University of Maryland Baltimore County, chemistry and biochemistry Hahm, Jong-in; Georgetown University, Department of Chemistry

Single Nanomaterial Level Investigation of ZnO Nanorod Sulfidation Reaction via Position Resolved Confocal Raman Spectroscopy

*Matthew Hansen[†], Johnson Truong[†], Brian Szychowski[‡], Tian Xie[†], Marie-Christine Daniel[‡], and Jong-in Hahm[†,]**

[†]Department of Chemistry, Georgetown University, 37th & O Sts. NW., Washington, DC 20057

[‡] Department of Chemistry and Biochemistry, University of Maryland Baltimore County, 1000 Hilltop Circle, Baltimore, MD 21250

**Address Correspondence to jh583@georgetown.edu*

ABSTRACT

Zinc oxide (ZnO) nanomaterials have been used as desulfurizing sorbents for gaseous streams, zinc sulfide (ZnS)-forming template lattices in nanomaterial synthesis, and agriculturally produced sulfur (S)-removing reagents from the environment. Although various nanoscale forms of ZnO are already utilized widely for such purposes, there is currently a lack of fundamental insight into sulfidation of ZnO nanomaterials provided at the single nanocrystal level. We demonstrate that position-resolved confocal Raman spectroscopy can be successfully used to reveal the sulfidation process of ZnO NRs occurring at the single nanomaterial level. We attain single crystal level understanding on facet-dependent sulfidation reactivity of ZnO NRs by tracking the same NRs with Raman spectroscopy before and after sulfidation reaction and quantitatively analyzing various ZnS-induced phonon scattering intensities from different positions on the NRs. The trend in NR facet-dependent sulfidation reactivity is further substantiated by correlating with the electron microscopy and fluorescence data measured from the same NRs. Insight from this study may provide a much-needed fundamental knowledge base for designing optimal ZnO nanostructures beneficial to many technological and industrial applications exploiting the ZnO to ZnS conversion. Taken together with the well-established methods to synthesize ZnO nanomaterials of specific crystal shapes and structures, our findings from the study may be broadly applicable in formulating and optimizing more advanced, low-dimensional ZnO sorbents and scrubbers for highly effective S removal.

Keywords: zinc oxide, zinc sulfide, nanomaterial conversion, sulfidation, crystal facet reactivity, Raman spectroscopy, electron microscopy, energy-dispersive X-ray spectroscopy, luminescence

Introduction

The conversion of zinc oxide (ZnO) to zinc sulfide (ZnS) is an important process in many technological and industrial applications such as optoelectronics, photocatalysis, gas sorbent, and gas removal.[1-11] For developing technologically useful materials, the conversion reaction has been exploited to synthesize one of the important wide-bandgap semiconductors of ZnS from a pre-made template of ZnO via reaction with hydrogen sulfide (H_2S)-generating reagents such as thioacetamide (TAA), sodium sulfide (Na_2S), and ammonium polysulfide ($(NH_4)_2S_x$).[1-4,12-17] In industrial and agricultural processes, important uses of this conversion reaction involve ZnO-based sorbents for removing H_2S in syngas production[5-9] and controlling the release of biogas-derived H_2S to the atmosphere.[10,11]

In particular, due to the enhanced sensing and catalytic functionalities that can be enabled by ZnS materials with reduced dimensionality,[1] nanoscale forms of ZnO have been extensively utilized as sacrificial templates for conversion to ZnS nanostructures. For example, different nanoscale ZnO structures have been identified as S-scrubbers,[10,11,18,19] even leading to commercially available, ZnO nanomaterial-based, S-sorbent products.[20,21] The use of nanosized ZnO in these applications has shown great promise as the inherently large surface-to-volume ratio of the nanomaterials offers higher conversion to ZnS than micron or bulk scale ZnO.[1] However, there still lacks fundamentally-driven guiding principles for selecting one type of nanomaterials over the others for ZnO sulfidation and the majority of current approaches to study the conversion of ZnO to ZnS relies on ensemble-averaged, macroscopic scale characterization methods or reactor-scale product testing. Sulfidation reaction of ZnO nanomaterials, therefore, has yet to be examined more systematically, especially at the individual nanomaterial level.

Different reactivities of ZnO materials towards sulfidation have been reported, but with mixed outcomes.[2,12-15,22] When ZnO sulfidation was carried out with $(NH_4)_2S_x$, it was found that the (0001) surface was the least reactive to sulfidation with the (000-1) and (10-10) surfaces reacting similarly better.[15] No appreciable morphological changes of ZnO were observed in this case. In another study of

ZnO reaction assisted with $(NH_4)_2S_xO_y$ and Na_2S, a significant change in ZnO structure was yielded after sulfidation.[16] Another body of studies, involving a starting material of ZnO or ZnTiO and a sulfidation agent of TAA[12,22] or H_2S gas at elevated temperatures,[13,14] reported that the (0001) surface was the most reactive towards sulfidation. In these works, considerable deformation of the starting ZnO material was detected.[12-14,22,23] Comparatively, very few studies exist that elucidate sulfidation reaction taking place on individual ZnO nanomaterials. Distinct from many past efforts using large-scale, ensemble-averaged evaluation of ZnO sulfidation reaction,[8-10,18-20] a chemically sensitive measurement approach capable of examining individual ZnO nanostructures and quantitatively providing information on crystal facet-specific sulfidation reaction will be highly beneficial in this regard.

Raman spectroscopy represents a powerful tool for probing chemical and structural changes of nanomaterials. Unlike electron microscopy (EM)-based techniques, Raman scattering can detect composition- and structure-associated material changes in various surrounding media. Despite this, the utility of Raman scattering for discerning facet-dependent chemical reactivities from discrete ZnO nanostructures has not been demonstrated yet.

In this work, we demonstrate that spatially resolved confocal Raman spectroscopy can be exploited to unambiguously reveal the different facet-dependent reactivities in the sulfidation of ZnO nanorods (NRs). ZnO NRs were selected for study due to the wealth of knowledge available, allowing for facile synthesis of well-defined and defect-free single crystals using chemical vapor deposition (CVD).[24-28] Individual ZnO NRs produced with high optical quality and well-defined crystalline structures can provide an ideal scaffold to elucidate ZnO facet-dependent reactivity differences towards sulfidation. We quantitatively determine NR facet-dependent sulfidation reactivities by resolving newly appearing ZnS Raman peaks measured from different NR positions on the same ZnO NRs and subsequently comparing the intensities of various ZnS phonon peaks from different facets. The Raman results are further supported by electron microscopy and fluorescence emission data obtained from the same NRs. Our efforts in this work can provide single crystal level understanding of facet-dependent S reactivity of ZnO NRs whose insight, in

turn, may lead to fundamentally guided, nanomaterial design principles important for the aforementioned applications. Together with the fact that ZnO nanomaterials can be made in a variety of shapes and crystal structures, our endeavors in this work can be broadly beneficial to meet the ever increasing demand for ZnO-derived nanomaterials in adsorption, removal, conversion, and separation of H_2S.

Experimental Methods

The synthesis of ZnO NRs was performed via CVD in a customized horizontal tube furnace. The feedstock source, a 2:1 by weight mixture of ZnO (99.999% purity) and graphite (99.99% purity) powders obtained from Alfa Aesar Inc. (Haverhill, MA), was placed in a source quartz boat and positioned on top of a heating element located at the center of the tube furnace. A target quartz boat containing the growth substrate, a 1 x 1 cm^2 Si wafer received from Silicon Quest, Inc. (San Jose, CA), was placed 15.6 cm away from the source boat, downstream from the Ar carrier gas flow. The Si wafer was pretreated with 20 μL of a growth catalyst, 20 nm Au colloid from Ted Pella, Inc. (Redding, CA), for 5 min. Subsequent thermal reduction of the feedstock source was achieved by heating the furnace to 950 °C for 20 min to 1 h at a ramp-up/ramp-down rate of 15 °C min^{-1} under a constant Ar gas flow of 100 standard cubic centimeters per minute.

Conversion of ZnO NRs to ZnS was carried out using thioacetamide (TAA), obtained from Sigma Aldrich Corp. (St. Louis, MO), dissolved in deionized water (DI) to a desired concentration of 0.002 to 0.2 M. Either densely grown ZnO NRs (referred as dense NR plate method) or dispersed ZnO NRs (dispersed NR reaction method) on a Si substrate were reacted by submerging the plate in 1 mL of TAA solution in a sealed tube. The sample was left to react at 90 ^oC for 24 h, after which it was rinsed with DI and subsequently dried under nitrogen. For attaining the different degrees of sulfidization reaction described in this paper, the concentration of TAA was adjusted while keeping the reaction time as 24 h. NR reactions with 0.002 M, 0.02 M, and 0.2 M of TAA yielded mildly, moderately, and highly sulfidated NRs, respectively. Regardless of the NR preparation protocol used, our measurements were focused on

collecting data from individual NRs. To achieve this, in the dense NR plate method, the densely grown mat of ZnO NRs on the growth substrate was first reacted with TAA. Subsequently, the TAA-reacted NRs were sonicated off from the original plate and redispersed onto a clean Si substrate for subsequent NR characterization. In the dispersed NR method, the NRs were initially sonicated off from the growth substrate containing dense ZnO NRs and dispersed in ethanol. Reconstituted ZnO NRs were then deposited onto a clean, gridded Si plate via drop-casting to track the same NRs during repeated measurements. All presented data showing the changes before and after TAA reaction by tracking the same NRs were obtained from the dispersed NR reaction method.

Morphological structures of the unreacted as well as S-reacted ZnO NRs were characterized using a field emission scanning electron microscope (FESEM), FEI Nova NanoSEM 450 (FEI Company, Hillsboro, OR), operated at 20 keV. Scanning tunneling electron microscope (STEM) images and energy-dispersive X-ray spectroscopy (EDX) data were also acquired on the same instrument using a STEM and EDX detector, respectively, by operating with a voltage of 30 keV. EDX data was then analyzed using AZtecTEM software from Oxford Instruments (Concord, MA). For STEM and EDX, TAA reacted NR samples were first prepared by the dense NR plate method described above. A 5 μL of the reacted NRs, resuspended in ethanol via sonication, was then deposited onto a TEM grid of a pure C film on 200-mesh Au (Electron Microscopy Sciences, Hatfield, PA). For all optical measurements, a Zeiss Axio Imager A2M (Carl Zeiss, Inc., Thornwood, NY) microscope equipped with an AxioCAM HRm digital camera was employed. Reflected bright/dark-field (BF/DF) illumination and unpolarized fluorescence excitation were produced using a 12V/100 W halogen lamp and a 120 W mercury vapor lamp (X-Cite 120Q), respectively. The wavelength range used for the fluorescence measurements was 450-490 nm for excitation and 510-540 nm for collection. BF, DF, and fluorescence images were acquired with EC Epiplan-NEOFLUAR 50X (numerical aperture, NA = 0.8) and 100X magnification (NA = 0.9) objective lenses using a 2 s exposure. X-ray diffraction (XRD) measurements were made using a Rigaku Ultima IV

X-ray diffractometer (The Woodlands, TX), operated with an accelerating voltage of 40 kV under Cu Kα radiation (1.542 Å) that scanned in the range of 2θ = 20-55° at a rate of 1 °/min.

Raman scattering data were collected using a LabRAM HR Evolution confocal Raman microscope (Horiba Instruments Inc., Sunnyvale, CA). The scattering data were obtained through a 100X magnification, long working distance, objective lens of NA = 0.8 (Olympus Corp., Waltham, MA) using a 100 mW 532 nm laser or, alternatively a 40 mW 405 nm laser, that was focused to an approximate beam size of 1 μm. The polarization of the incident laser ($\mathbf{E_{inc}}$) was kept perpendicular to the NR long axis (c-axis), i.e. NR $\perp$ $\mathbf{E_{inc}}$, for all Raman data of the individual NRs reported in the paper. Raman scattering signals were then collected using an 1800 line per mm grating and a charge-coupled-device (CCD) detector. The scan range used was 50-500 cm^{-1} and 125-500 cm^{-1} for the 532 nm and 405 nm laser, respectively. The stated frequency window was chosen to examine the characteristic Raman fingerprint regions for the materials of ZnO and ZnS, while considering the filter specifications used in our experimental setup for the two excitation lasers.

Results and Discussion

We first acquired ensemble-averaged data collectively from many ZnO NRs. Figure 1 displays the Raman, fluorescence, and XRD data obtained from the different TAA reaction stages of densely grown ZnO NRs on a Si growth plate, undergoing from unreacted, to mildly reacted, and to extremely reacted stages in Figures 1(A), 1(B), and 1(C), respectively. The image inserted above the Raman spectrum in Figure 1(A) displays a BF view of a densely grown mat of ZnO NRs on Si. The typical Raman spectrum of unreacted ZnO NRs as-grown on Si is provided in Figure 1(A). The Raman peaks at 98, 331, 378, 413, and 437 cm^{-1} correspond to the E_{2L}, 2nd order E_{2H}-E_{2L}, A_{1T}, E_{1T}, and E_{2H} phonon modes, respectively. These peaks are the characteristic Raman modes associated with ZnO exhibiting a wurtzite crystal structure of the C^4_{6v} space group.[29,30] This symmetry group has six 1st order optical modes (Γ_{opt} = A_1+2B_1+E_1+2E_2 at the Γ point of the Brillouin zone (BZ)), consisting of A_1, B_{1L}, B_{1H}, E_1, E_{2L}, and E_{2H}.

Of these, all but the two B_1 modes are Raman active. With further reaction of the ZnO NRs with TAA, new Raman peaks emerged that were consistent with the presence of ZnS. The Raman spectrum in Figure 1(B) from the moderately reacted ZnO NRs now displays peaks from both ZnO and ZnS. The new peaks at 150, 261, and 349 cm^{-1} belong to ZnS. The broad shallow peak centering at 150 cm^{-1} is associated with multiple 2nd order Raman modes such as $2TA_L$, $[TO_u\text{-}LA]_\Sigma$, $[LO\text{-}LA]_\Sigma$, and $2TA_X$.[31-33] Another broad peak spanning the frequency of 240 to 285 cm^{-1} stems from both the 1st order (three weak phonon modes of A_{1T}, E_{1T}, and E_{2H}) and 2nd order (contributions from acoustic overtones such as $[2TA_u]_\Sigma$, $[LA+TA_l]_W$, and $[LO\text{-}TA_u]_X$) ZnS peaks.[31-33] T, L, A, and O stand for the transverse, longitudinal, acoustic, and optic modes. The subscripts of u and l indicate the upper and lower branch of the mode, respectively, whereas those of Σ, W, and X denote the different symmetry points in BZ. The peak appearing at 349 cm^{-1} is a contribution from the co-located, 1st order A_{1L}/E_{1L} modes.[29,34] The spectrum in Figure 1(B) also shows an additional ZnS peak in the frequency region of 275-283 cm^{-1} that matches the predicted Raman shift region of the weak ZnS phonon modes of A_{1T}, E_{1T}, and E_{2H}.[34] However, due to the close proximity and weak signal of these phonon modes, we cannot distinguish the exact peak location for each mode. As such, we report them as a range indicating a combined peak contribution of all three modes. At the same time, ZnO signals are also present in the Raman spectra of the moderately reacted NR ensemble sample. The E_{2L} and E_{2H} modes of ZnO still remained as pronounced. The minor ZnO modes of $E_{2H}\text{-}E_{2L}$ and A_{1T}/E_{1T} under this light interaction geometry were still identifiable. The peak near 334 cm^{-1} is a combined contribution from the surface optic (SO) mode of ZnS.[35] Lastly, the Raman spectrum of the fully reacted NRs is shown in Figure 1(C). The NRs underwent near complete sulfidation which can be seen by the negligible presence of the ZnO-related Raman peaks. Rather, in the extremely reacted NRs, ZnS signals were prominently observed, particularly from the higher order peaks at 150 cm^{-1} and 261 cm^{-1}. In addition, another dominant ZnS peak appeared at 349 cm^{-1}, which is due to combined contributions of A_{1L} and E_{1L} modes of ZnS.[34] Table 1 summarizes these different phonon modes that were resolved in our Raman measurements of the unreacted and S-reacted ZnO NRs.

Peak location (cm^{-1})	Phonon mode assignment	Peak feature	ZnO or ZnS
70*	E_{2L}(h)	medium	ZnS
98*	E_{2L}	intense under NR ⊥ $\mathbf{E_{inc}}$	ZnO
150	2nd order multiple optic and acoustic overtones	broad, spanning 130-180 cm^{-1}	ZnS
261	2nd order multiple optic and acoustic overtones	broad, spanning 240-270 cm^{-1}	ZnS
275-283	E_{1T}(h), A_{1T}(h), T_{2T}(c) E_{2H}(h)	weak	ZnS
331	2nd order E_{2H}-E_{2L}	weak	ZnO
334	SO(h,c)	weak	ZnS
340-360	E_{1L}(h), A_{1L}(h), T_{2L}(c)	medium to strong	ZnS
378	A_{1T}	weak under NR ⊥ $\mathbf{E_{inc}}$	ZnO
413	E_{1T}	weak under NR ⊥ $\mathbf{E_{inc}}$	ZnO
437	E_{2H}	intense under NR ⊥ $\mathbf{E_{inc}}$	ZnO

Table 1. Measured frequencies of 1st and 2nd order Raman peaks pertinent to sulfidation of ZnO NRs. Phonon modes associated with ZnO and ZnS are shown in clear and shaded elements, respectively. ZnS Raman modes corresponding to the crystal phases of hexagonal wurtzite and cubic zinc blend are indicated as (h) and (c), respectively. The two lowest frequency peaks marked with * were observed only under 532 nm excitation due to our instrument setup allowing frequency detection greater than 125 cm^{-1} with 405 nm excitation.

The image panel to the right of each Raman spectra in Figures 1(A through C) displays the corresponding fluorescence emission data of the NR ensemble sample. The fluorescence panel of the as-synthesized ZnO NRs in Figure 1(A) is completely dark. This is as expected from high purity ZnO NRs grown using CVD,[27,28,36] which show negligible chemical and crystalline defects. In contrast, ZnO NRs

after TAA reaction in Figures 1(B) and 1(C) display considerable green emission. The green fluorescence stems from sulfidation-caused atomic and structural defects that started developing in the original ZnO NR crystal. Similar defect-originated luminescence in the visible range has been well-documented from ZnO and is known to be associated with atomic point defects in the material such as interstitial and vacancy sites.[37-39] As the reaction proceeded towards near completion, the intensity of the green fluorescence also increased, as evidenced by comparing the fluorescence panels shown in Figures 1(B) and 1(C). Corroborating the trend in ZnS-associated Raman signals in the Raman spectra in Figure 1, the higher fluorescence emission found in Figure 1(C) relative to that of Figure 1(B) indicates that fluorescence intensity is correlated to the level of NR sulfidation.

Figures 1(D) through 1(E) display the XRD data for both the unreacted, moderately reacted, and extremely reacted ZnO NR ensemble samples. The diffraction peaks of the as-grown, dense mat of ZnO NRs on Si are presented in the XRD spectrum in Figure 1(D). Characteristic wurtzite ZnO (JCPDS PDF card no. 36-1451) peaks of (10-10), (0002), (10-11), and (10-12) appear at approximately 2θ = 31.8°, 34.5°, 36.5°, and 47.5°, respectively. Figure 1(E) displays the XRD pattern of the NR ensemble sample after a moderate reaction with TAA. The XRD spectrum after TAA reaction exhibits a new small peak at approximately 28.5°, corresponding to ZnS (JCPDS PDF card no. 36-1450). In addition, the (11-20) peak of ZnS at 47.5° appears at the same positions as (10-12) of ZnO, as indicated in Figure 1(E). As the reaction was proceeded to near completion, the two ZnS-associated diffraction peaks of (10-10) and (11-20) at 28.5° and 47.5°, respectively, increased their intensities substantially relative to the ZnO diffraction peaks, as shown in Figure 1(F).

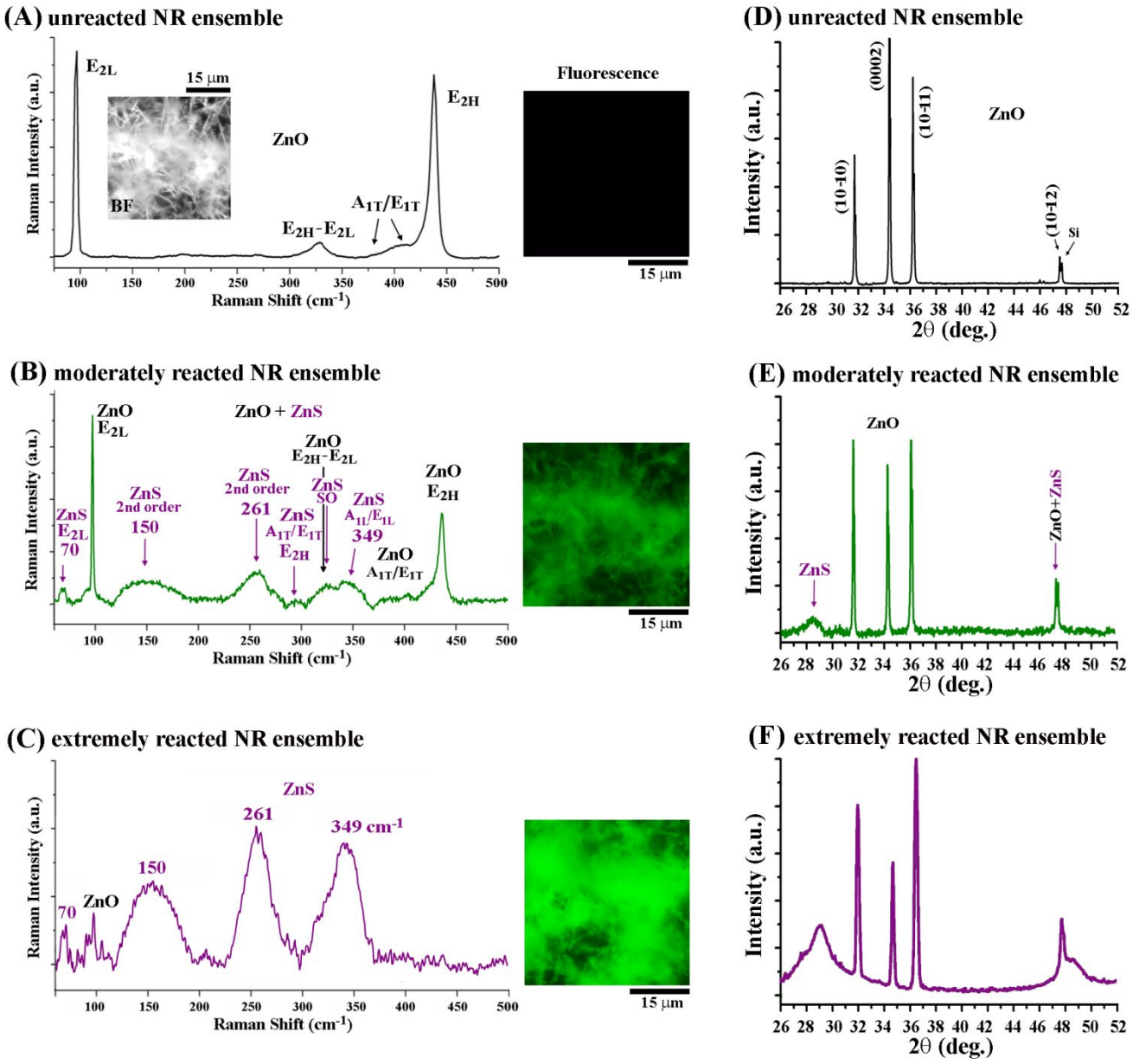

Figure 1. Raman scattering, fluorescence, and X-ray diffraction (XRD) data of a dense mat of ZnO NR ensemble sample taken after varying degrees of TAA reaction. **(A through C)** Raman scattering spectra and fluorescence emission panels were obtained from an (A) unreacted, (B) moderately reacted, and (C) extremely reacted ZnO NR ensemble sample. An exemplar BF panel of a dense mat of ZnO NR ensemble as-synthesized is inserted in (A). Raman scattering measurements were carried out with 532 nm incident light. Fluorescence data of the samples were collected by using $\lambda_{excitation}$ = 450-490 nm and $\lambda_{collection}$ = 510-540 nm. (A) Raman scattering profiles of the pristine ZnO NRs show the characteristic

ZnO phonon peaks of E_{2L}, E_{2H}-E_{2L}, A_{1T}, E_{1T} and E_{2H}, as annotated in the spectrum. No fluorescence emission was seen from these pristine ZnO NR ensembles. (B) When moderately reacted with TAA, the Raman scattering spectrum of the ZnO NR ensemble sample exhibits peaks associated with both ZnO and ZnS. Pertinent ZnO and ZnS phonon modes are annotated next to each peak in the spectra. Considerable green fluorescence was emitted from the moderately reacted sample. (C) When the ZnO NR ensemble sample was reacted to near completion, ZnS peaks dominated the Raman spectrum with negligible peak presence of ZnO. The extremely reacted sample showed intense green fluorescence. **(D through F)** XRD patterns of the (D) unreacted, (E) moderately reacted, and (F) extremely reacted ZnO NR ensemble sample. (D) Diffraction peaks belonging to pure ZnO NRs are annotated in the XRD spectra. (E) A new peak at ~29° belonging to ZnS appeared after moderate TAA reaction. All characteristic ZnO diffraction peaks are still largely retained in the XRD spectra, one of which shares the same peak location as ZnS, as assigned in the spectra. (F) The ZnS-associated diffraction peaks grew stronger in intensity in the extremely reacted sample.

We continued the structural and chemical investigations of ZnO NRs while focusing on individual NRs instead of their ensembles. Figure 2(A) shows an illustration of collecting spatially resolved Raman scattering signals along the different positions on single NRs. The excitation polarization was held perpendicular to the long axis (c-axis) of the NR, whose light-matter interaction geometry is known to provide the most sensitivity from ZnO NRs with the intense and dominant E_{2L} and E_{2H} signals.[40,41] Although much lower in intensity under this light-matter interaction orientation, additional ZnO phonon modes such as E_{1T}, A_{1T}, and the 2nd order E_{2H}-E_{2L} are also expected to be present according to the selection rule. The molecular origins of the vibrations associated with the allowed ZnO Raman modes are schematically depicted using a ball-and-stick model in Figure 2(A). Figure 2(B) displays a SEM image of

a single, unreacted ZnO NR as well as its spatially resolved Raman spectra collected using a 532 nm laser. Raman measurements were performed from two distinctive positions of NR middle (blue) and end (red) to ascertain the reactivity differences associated with the side (prismic) and end (basal) facets of a ZnO NR, respectively. Both the SEM micrograph and the Raman spectra presented in Figure 2(B) are typical of pristine, individual ZnO NRs before TAA reaction. The two end facets of wurtzite ZnO NR crystals consist of the purely Zn-containing (0001) and O-containing (000-1) planes in contrast to the six side facets of {10-10} planes on the NR main body that have an equal surface density of Zn and O atoms due to the alternating Zn and O layers in the crystal. The SEM micrograph of the unreacted ZnO NR in Figure 2(B) shows that the NR indeed exhibits clean and smooth hexagonal facets at the two ends and rectangular facets on the six sides of the wurtzite crystal. The corresponding Raman scans in Figure 2(B) display the two dominant ZnO phonon modes of E_{2L} and E_{2H} from both the NR middle and end locations. The spectra also show other allowed modes of E_{1T}, A_{1T}, and E_{2H}-E_{2L}, as discussed above.

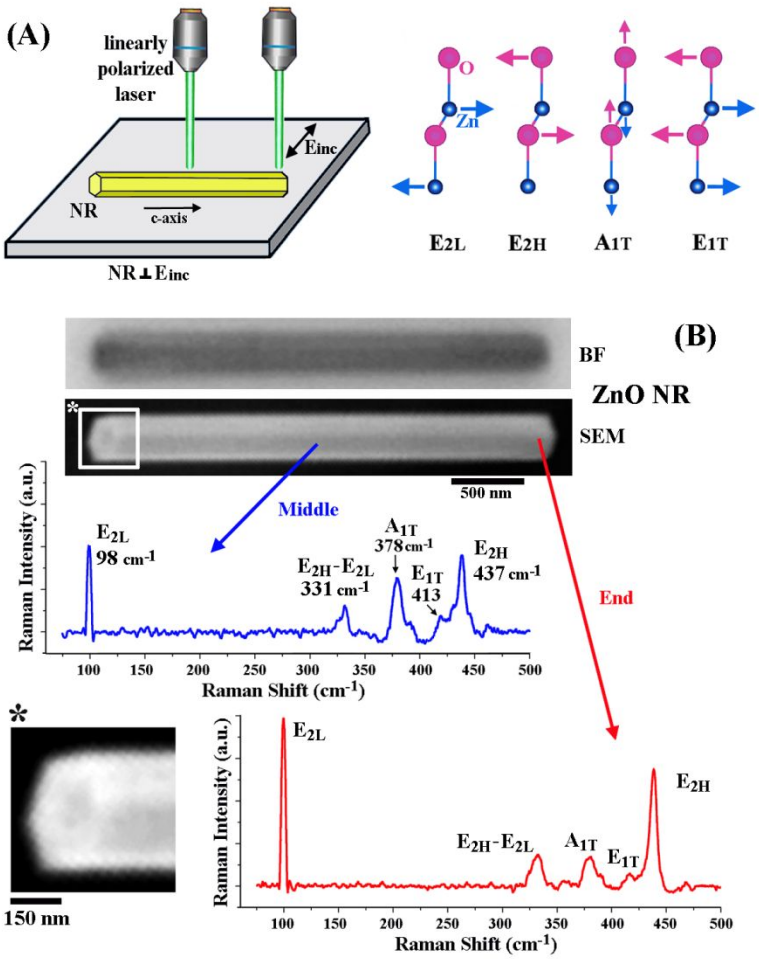

Figure 2. **(A)** The schematic illustration depicts the position-resolved Raman scattering measurements focusing on individual ZnO NRs using a linearly polarized laser ($\mathbf{E_{inc}}$) with its excitation polarization oriented perpendicular to the NR long axis, i.e. c-axis. All allowed Raman active modes expected from a wurtzite ZnO crystal are depicted using a ball-and-stick model, displaying the different vibrations associated with the Zn and O atoms for each phonon mode. **(B)** Typical SEM panel and Raman spectra obtained from unreacted, individual ZnO NRs are displayed. The grey scale SEM image shows the basal and prismic facets of a wurtzite ZnO NR crystal where the NR region marked with an asterisk is also provided as a zoomed-in SEM inset. The BF panel represents the typical optical image of pristine ZnO NRs viewed under the confocal Raman microscope to focus the laser beam on a specific point along the NR long axis such as the middle or end position. The blue and red Raman spectra correspond to the scattering signals measured at the middle and end positions, respectively, of the ZnO NR shown in the

SEM panel. 532 nm incident light was used for Raman scattering collected at the Raman shift window of 70-500 cm^{-1}. ZnO Raman peaks corresponding to the E_{2L} (98 cm^{-1}), E_{2H}-E_{2L} (331 cm^{-1}), A_{1T} (378 cm^{-1}), E_{1T} (413 cm^{-1}) and E_{2H} (437 cm^{-1}) modes were detected in both spectra which, under this light-matter interaction geometry of NR $\perp$ $\mathbf{E_{inc}}$, show the two E_2 peaks (E_{2L} and E_{2H}) as the dominant ZnO phonon modes.

We then investigated the effect of TAA reaction on single ZnO NRs prepared by the 'dense NR plate' method where the as-synthesized ZnO NRs were first reacted with TAA on the Si growth substrates. Subsequently, the TAA-reacted ZnO NRs were sonicated off and redeposited onto a clean Si plate for the ensuing optical, fluorescence, SEM, and Raman measurements of single NRs. As the NR data in Figures 3 through 5 were created this way, the reactivities on the two NR ends were not identical to each other. Only one end of the NRs was freely exposed to the TAA solution whereas the other end was anchored to the underlying growth plate and partially buried by the neighboring NRs. Despite this, a general trend in S reactivity was observed between the NR middle and end positions.

A representative set of BF, SEM, fluorescence, and Raman data was obtained from single ZnO NRs that underwent a mild sulfidation reaction with TAA, as shown in Figure 3. The SEM panel in Figure 3(A) reveals that the sulfidation reaction resulted in the formation of small nodules decorating the surface of a NR. The inset marked with an asterisk in Figure 3(B) further shows a zoomed-in SEM view of these nanoparticles (NPs) of ~35 nm in diameter produced on the mildly reacted ZnO NR. Similar ZnS particles have been previously reported to form outside ZnO voids via the Kirkendall effect.[12,14,22] The fluorescence panel in Figure 3(A) shows green emission present continuously on all positions along the length of the NR. NR position-resolved Raman spectroscopy was subsequently performed under 532 nm excitation. Figure 3(B) displays the resulting Raman spectra. The exact positions on the NR from which

the Raman spectra were obtained are marked using the SEM viewgraph of the NR. In both the Raman spectra acquired from the middle (blue) and end (red) positions, the dominant signals were the E_{2L} and E_{2H} modes of ZnO. In addition to the ZnO peaks, a small hump at around 70 cm^{-1} newly appeared in both Raman spectra after mild TAA reaction. The peak is due to the E_{2L} mode of ZnS formed via the chemical conversion of ZnO to ZnS, as shown below.[14] H_2S released after the hydrolysis reaction of TAA further reacts with ZnO NRs and converts ZnO to ZnS, an energetically favored process with -87.9 kJ/mol at 90 °C.

$$CH_3CSNH_2\ (TAA) + H_2O \rightarrow CH_3CONH_2 + H_2S$$

$$CH_3CSNH_2 + 2H_2O \rightarrow CH_3COOH + NH_3 + H_2S\ (\text{or } CH_3COONH_4 + H_2S)$$

$$ZnO\ (s) + H_2S\ (aq) \rightarrow ZnS\ (s) + H_2O\ (l)$$

Figure 3(C) displays typical STEM and EDX data collected from NRs after sulfidization. The EDX spectrum of a NR shown in the STEM panel in Figure 3(C) is presented along with the EDX images that contain the elemental mapping results for Zn, O, and S. These results agree with the Raman outcomes and confirm the presence of the three atomic elements on the NR after undergoing the sulfidation reaction shown above. Further, the EDX maps of the NR qualitatively show the spatial distribution of Zn, O, and S in the NR. O is found in the NR interior, showing a weaker presence in the NR exterior. On the contrary, S, along with Zn, is found both in the interior as well as the exterior of the NR where more S is positioned near the exterior. The distribution of Zn, O, and S in a sulfidized NR can be more clearly seen in the overlapped channels of EDX chemical maps provided in ESI, Figure S1†.

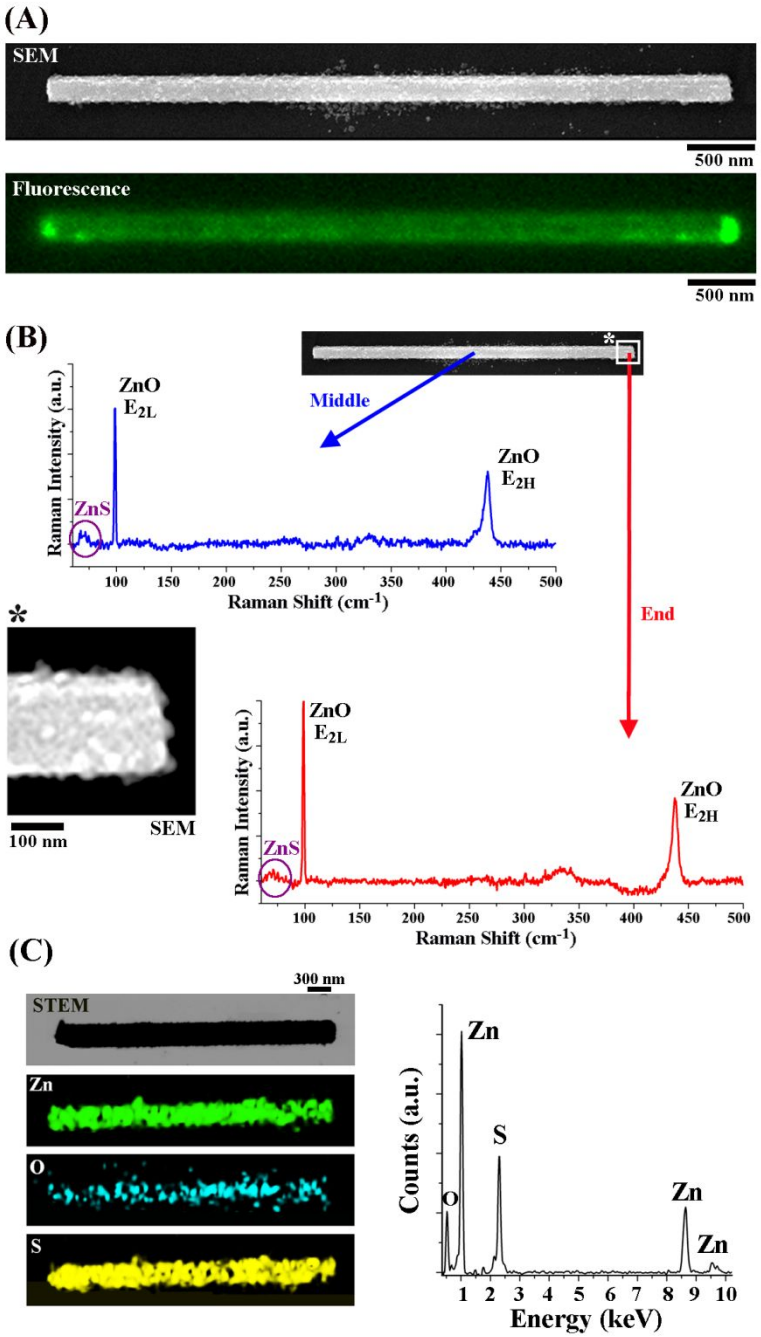

Figure 3. A representative set of correlated SEM, fluorescence emission, and Raman scattering data from mildly sulfidated ZnO NRs. **(A)** The SEM panel of a ZnO NR after mild reaction clearly displays small NPs of ~35 nm in diameter decorating the outer surface of the still largely intact NR. In contrast to the complete absence of fluorescence seen from unreacted ZnO NRs, green fluorescence was noticeable from all positions of the mildly reacted NR. **(B)** Raman spectra taken at the middle (blue) and end (red) positions of the NR discussed in (A) are presented. The incident laser used was 532 nm with its

polarization perpendicular to the NR c-axis. The exact NR positions from which the presented spectra were obtained are indicated in the SEM image. The zoomed-in SEM view of the NR region marked with an asterisk is also shown. Overall, the Raman scattering data from both NR positions indicated that the NR with the strong E_{2L} and E_{2H} ZnO peaks is still largely made up of ZnO. At the same time, the presence of ZnS in the NR was confirmed with a small peak newly appearing at 70 cm^{-1} that corresponds to the E_{2L} mode of ZnS. **(C)** STEM/EDX data of a ZnO NR after mild sulfidization reaction. The grey scale panel corresponds to the STEM viewgraph of the NR whose chemical compositions and their spatial distributions were subsequently assessed by EDX measurements performed on the NR. The green, blue, and yellow channels display the EDX maps of the NR corresponding to the atomic element of Zn, O, and S, respectively.

A representative data set obtained from moderately reacted ZnO NRs is displayed in Figure 4. The morphology of a moderately reacted NR revealed by SEM in Figure 4(A) confirms that the ZnO NR was subject to more substantial reaction around the NR side and end facets. The speckled ZnS NPs on the NR surface seemed to have coalesced into a near complete shell, separated entirely from the core by a layer of a void region in some parts and into small cavities in other parts of the NR. Such shell and void structures of the NR can be more clearly seen in the zoomed-in SEM panel in Figure 4(B) for the NR combinedly examined with BF, SEM, fluorescence, and Raman as well as in the high magnification SEM data in Figure 4(C) acquired from similarly reacted NRs. Additional structural changes were observed all along the NR length where local dissolution of the NR seemed to have occurred. The NR side and end facets were no longer clean and smooth. The crystal in Figure 4(A) now appears tapered on the left end while the facets on the side and the right end have uneven, gnawed morphology. The fluorescence emission panel in Figure 4(A) shows that the fluorescence intensity is overall higher for the moderately reacted NR relative to the case in Figure 3(A). As discussed before, the fluorescence intensity profile along the NR

seemed to be consistent with the level of sulfidation-induced NR morphological change observed by SEM. The left end of the NR showing the higher fluorescence emission belongs to the more disrupted NR end with greater degradation and loss of its original facet structure in the SEM panel. The Raman spectra of the moderately reacted ZnO NR provided in Figure 4(B) resolve the scattering signals from the NR middle (blue) and end (red) positions as marked in the SEM image. The ZnS E_{2L} peak at 70 cm^{-1} is more pronounced than the case in Figure 3(B). Furthermore, additional characteristic peaks of ZnS are now present such as the ones centering at 283 cm^{-1} and 349 cm^{-1} due to the combined contributions from multiple 1st order phonon modes as specified in Table 1. In addition, broad peaks are observed at 150 cm^{-1} and 261 cm^{-1} which belong to the 2nd order ZnS Raman modes as discussed earlier. Rather shallow and broad peaks located at 320-400 cm^{-1} are due to the combined contributions of ZnS and ZnO where the 2nd order ZnS peaks emerge together with the signals from the E_{2H}-E_{2L}, A_{1T}, and E_{1T} modes of ZnO, as annotated in the spectra. At the same time, the once dominant E_{2L} and E_{2H} peaks of ZnO are still quite noticeable, but their relative intensities compared to those of the ZnS E_{2L} and E_{2H} peaks now have been significantly diminished both in the middle and end spectra.

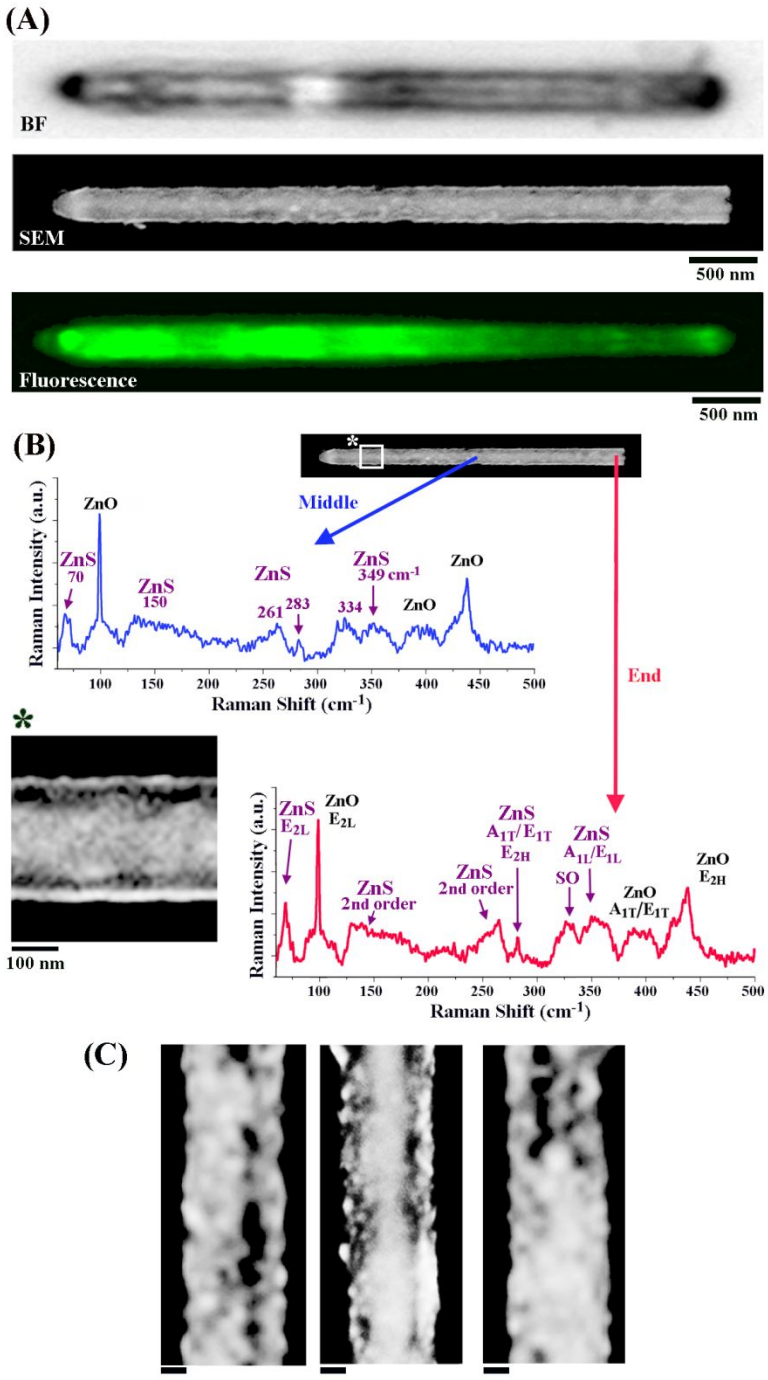

Figure 4. A representative set of correlated BF, SEM, fluorescence emission, and Raman scattering data from moderately sulfidated ZnO NRs. **(A)** The SEM panel of a moderately reacted ZnO NR reveals a shell-like structure that is separated from the NR core by a thin void layer formed just beneath the NR surface. Strong fluorescence emission was observed on all positions of the NR. **(B)** Raman scattering data of the moderately reacted NR are presented as two spectra, corresponding to the signals collected

from the middle (blue) and end (red) positions of the NR. An excitation wavelength of 532 nm was used with its polarization perpendicular to the NR c-axis. Overall, the Raman scattering peaks of the NR indicated the combined contributions of ZnO and ZnS. The ZnS E_{2L} peak at 70 cm^{-1} has grown substantially and additional ZnS peaks have developed at 150 cm^{-1}, 261 cm^{-1}, and 349 cm^{-1}. At the same time, the intensities of the two dominant ZnO modes of E_{2L} and E_{2H} have decreased considerably to the intensity levels of the minor ZnO peaks of E_{2H}-E_{2L}, A_{1T}, and E_{1T}. A zoomed-in SEM view of the NR region marked with an asterisk clearly displays the structural changes that the NR underwent during the sulfidation reaction, which yielded an outer shell separated from the core by a gap layer. **(C)** High magnification SEM images are additionally provided for NRs that underwent a moderate sulfidation reaction similar to the NR shown in (A and B). The additional NRs also exhibit shell-like structures due to the formation of void regions just beneath the NR surface. All scale bars are 100 nm.

The data set provided in Figure 5 represents highly sulfidated ZnO NRs. The ZnO NR in Figure 5 underwent significant reaction to the point of developing completely hollow regions in the NR, as seen in the SEM panel in Figure 5(A). The magnified SEM view in the inset of Figure 5(B) is presented to display the tube-like structure of the NR with no core material inside. Figure 5(C) presents high magnification SEM images taken from additional, highly reacted NRs in order to clearly show the tube-like structures formed inside highly sulfidized NRs. The fluorescence profile of the highly reacted NR in Figure 5(A) exhibits intense green emission to the largest extent of all the individual NR cases discussed so far. The Raman spectra from the middle (blue) and end (red) positions of the highly reacted NR in Figure 5(B) further confirm this increased level of ZnO to ZnS conversion. ZnO scattering signals from all phonon modes are found to be substantially weaker than the previous cases. Additionally, compared to the NR in Figure 4, there is generally a loss of ZnS spectral features. The reduction of not only ZnO but

also ZnS signals in the highly reacted NR sample may result from the overall material loss as well as the destruction of any ordered ZnO or ZnS structures that were previously present. Such loss of the NR matter and structural integrity is observed in the SEM panels in Figure 5 as the largely deformed NR ends and the hollow spaces formed in the NR. For ZnS Raman peaks, it is the higher order modes such as those at 150 cm^{-1} and 261 cm^{-1} that become more pronounced at this stage, rather than the 1^{st} order peaks. This is consistent with the results presented in Figure 1(C) where it was also the higher phonon modes of ZnS that were predominantly found in the more sulfidized NR ensemble sample.

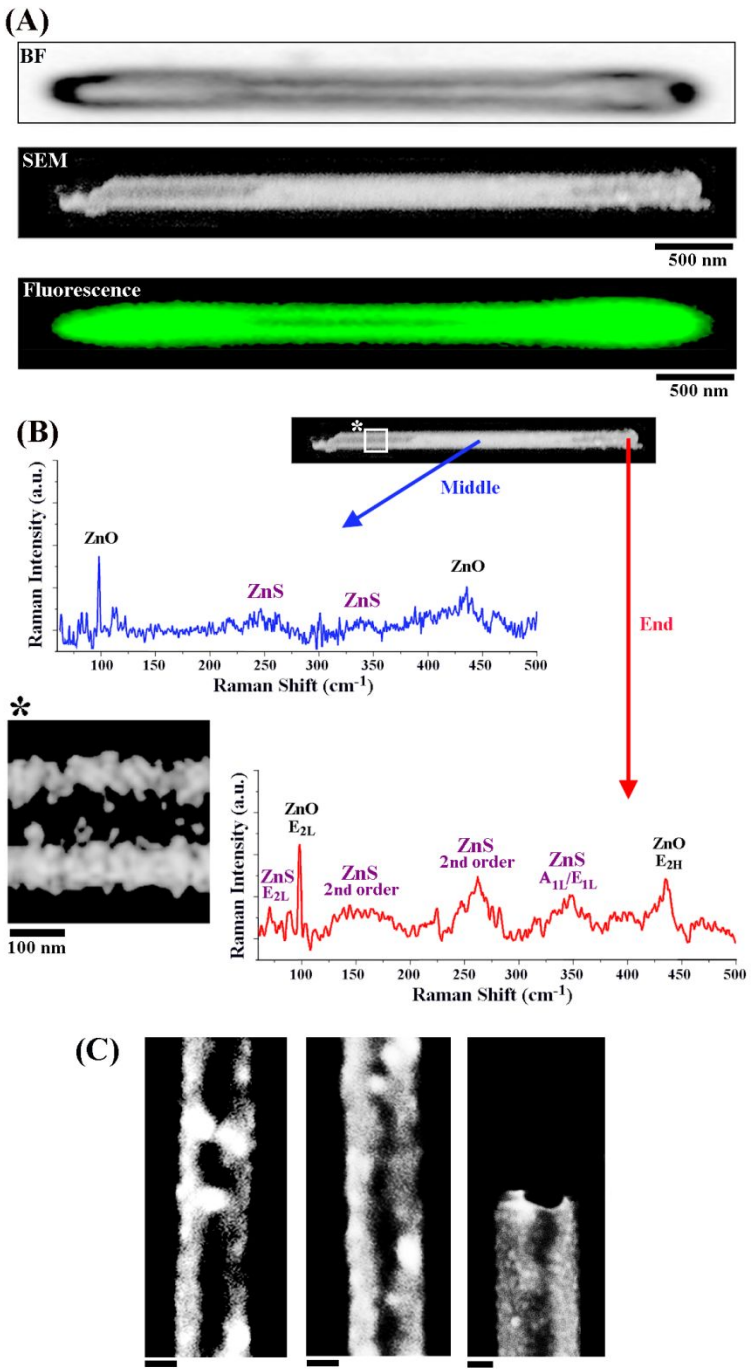

Figure 5. A representative set of correlated BF, SEM, fluorescence emission, and Raman scattering data from highly reacted ZnO NRs. **(A)** The SEM micrograph of a highly reacted ZnO NR indicates that the void regions seen in the moderately reacted NR in Figure 4 are no longer confined just beneath the NR surface and have penetrated into the core section in some parts of the NR, forming tube-like structures towards the two NR end regions. The fluorescence panel displays intense green emission along the NR.

(B) The corresponding Raman spectra of the highly reacted NR in (A) are presented. The spectra of the NR middle (blue) and end (red) positions were taken with 532 nm incident light with its polarization perpendicular to the NR c-axis. The grey scale image marked with an asterisk is the zoomed-in SEM viewgraph to show the hollow structure formed inside the highly reacted NR. Overall, both ZnO and ZnS signals were found to decrease in the highly reacted NR relative to the previous cases. As for the ZnS related Raman peaks, the higher order modes were found to be more persistent with more NR sulfidation. **(C)** Additional, high magnification SEM images are provided for highly reacted NRs. The characteristic, tube-like structures with no core materials inside the NR can be clearly seen from all panels. The scale bar under each panel is 100 nm in length.

When examining the effects of varying sulfidation degrees on the individual NR cases in Figures 3 through 5, higher sulfidation reactivity seems to be expected for the end (basal) than for the main body (prismic) facets of the ZnO NRs. Qualitatively from the combined fluorescence emission, SEM, and Raman data of the NRs at the various sulfidation stages, the NR end facets of {0001} seem more susceptible to the sulfidation reaction with H_2S than the side facets of {10-10}. From the view point of dangling bond scenario in wurtzite ZnO, the atoms on the end facets of the ZnO crystal are only bound to one atom in the underlying layers, leading to easier removal of the atoms at the end once the surface layer is disrupted. In contrast, the atoms on the main body (side) facets have alternating Zn and O atoms on the more stable surfaces of {10-10}, where the Zn and O atoms are attached to multiple adjacent atoms.[42] This would suggest that dissolution of ZnO by H_2S at the side facets can be favored over the end facet reaction only under circumstances of defect-triggered reaction.[12] However, the highly crystalline, optical quality ZnO NRs used in our experiments[27,28,41] ensured that the crystals were free of such defects on the

side facets which, in turn, make the end facets more vulnerable to the chemical reaction as explained above.

The mechanism of sulfidation reaction seen on the NRs in Figures 3 through 5 may be understood by S/Zn atoms diffusing into/out of the NRs. The S^{2-} from H_2S can react with Zn^{2+} on the ZnO NR surface, leading to the build-up of ~35 nm ZnS NPs on the NR in Figure 3. This initial ZnS NP formation is likely to be driven by the more thermodynamically stable ZnS formation energy and the lower solubility of ZnS in water compared to ZnO. The NR sulfidation reaction may then continue via a Kirkendall effect,[12,22] forming the void layer separating the outer ZnS shell from the inner ZnO core in Figure 4. Figure 4 also shows small gaps and channels appearing between the ZnS shell and the ZnO core, preserving contact points between the two materials. Those ZnO core parts still in physical contact with the ZnS shell may serve as transportation channels for Zn^{2+} ions to diffuse out and reach the reaction interface to further react with S^{2-} ions. As the sulfidation reaction proceeds, the ZnS shell continues to thicken since the smaller size of Zn^{2+} relative to that of S^{2-} will make the cations move readily through the ZnS shell to react with S^{2-} in solution. This Kirkendall process may lead to the eventual formation of a hollow space in the NR core observed in Figure 5, transforming the more reactive NR end facets and the neighboring NR parts to tube-like regions, leaving them only with thick ZnS shells.

We further investigated the ZnO NR facet-specific reactivity towards H_2S in a quantitative manner, while ruling out any geometric effects in sulfidation of the vertically oriented NRs on the growth substrate. Hence, for this set of experiments, we employed individual ZnO NRs prepared by the 'dispersed NR reaction' method. Lying flat on the reaction substrate in this case, all parts of individual ZnO NRs were allowed to equally react in TAA. We then characterized the sulfidized NRs to obtain spatially resolved Raman spectra under both 405 and 532 nm excitations. Furthermore, we systematically analyzed the intensities of the various ZnS phonon modes measured from both the middle and end positions of the same NRs and quantitatively determined the differences in the NR facet reactivity.

Figure 6 shows the summary bar graphs of the NR facet reactivity evaluated by spatially resolved Raman spectroscopy. The bar graphs in Figure 6(A) compare the Raman intensities of different ZnS peaks, one for the combined 2nd order modes at 261 cm^{-1} and the other for the A_{1L}/E_{1L} modes at 349 cm^{-1}, from the two distinctive positions on the NRs discussed in Figures 4 and 5. The results in the bar graphs show that ZnS signals are substantially higher for the NR end than for the middle of the same rods. EDX measurements and elemental analysis performed on the two distinct positions of a moderately sulfidized NR also showed a similar trend to the Raman results summarized in Figure 6(A), see Figure S1 in Supporting Information. To substantiate these findings, we profiled the Raman scattering behaviors of an additional set of 20 ZnO NRs prepared via the dispersed NR reaction method. Representative bar graphs from these measurements are shown in Figure 6(B) for 10 independent NRs. It is apparent from the data that, regardless of the excitation wavelengths used or particular ZnS Raman modes analyzed, higher Raman intensities of ZnS are found at the NR ends versus the middle. To verify the reactivity trends associated across the 20 NRs studied, we averaged the end versus middle data for the same NRs for the three characteristic ZnS peaks of 70, 261, and 349 cm^{-1} collected under 532 nm illumination. The Raman intensity values at the NR ends were obtained by considering only the higher intensity end of the two termini for the left panel in Figure 6(C), while the data shown in the right panel were resulted from considering the mean of the two NR end intensities. The middle and end intensity values were normalized to the end intensity in all cases. The outcomes were then constructed into bar graphs as displayed in Figure 6(C), which confirmed no substantial reactivity difference between the two NR termini. Clearly visible from all comparison graphs in Figure 6 is that the sulfidation-induced Raman signals are greater at the end versus the middle of the NR for all ZnS phonon mode and excitation cases. Hence, by quantitatively comparing the position-resolved Raman chemical fingerprinting data from the same NRs, we conclusively show that the conversion from ZnO to ZnS occurs more readily at the two ends than on the main body of the NR.

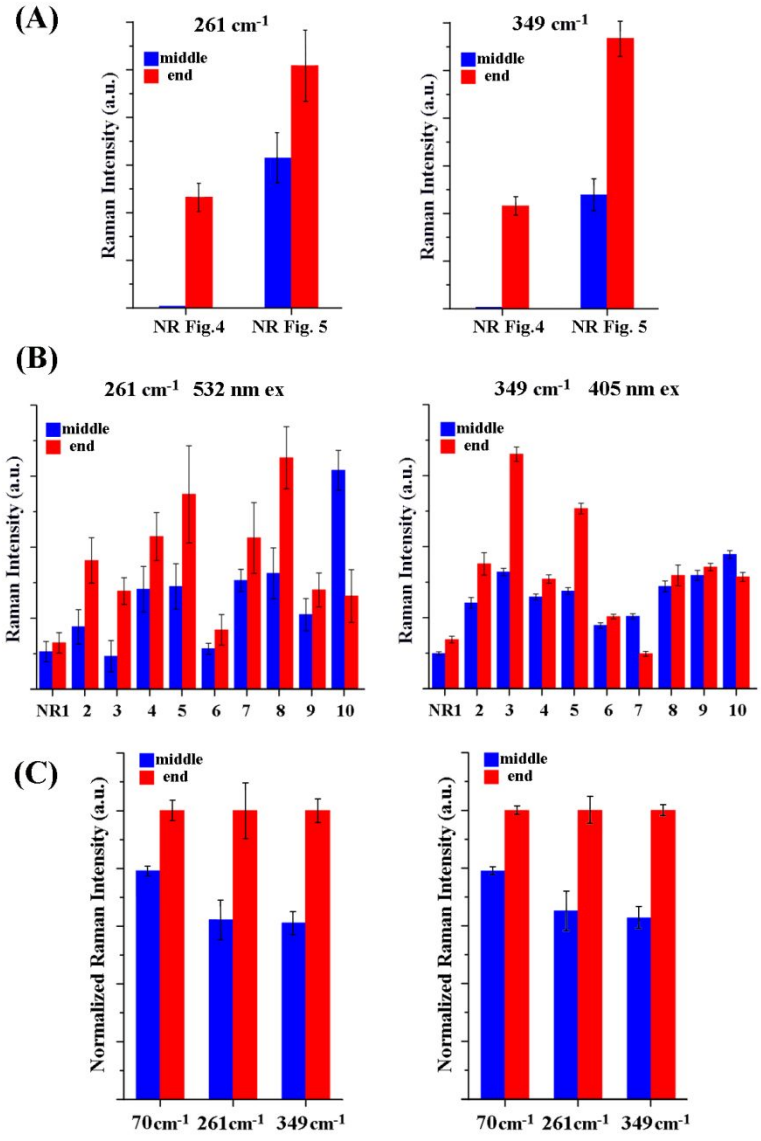

Figure 6. NR facet-specific sulfidation reactivity examined by position-resolved Raman scattering experiments on individual ZnO NRs. **(A)** The Raman intensities of the two ZnS phonon modes at 261 cm^{-1} and 349 cm^{-1} are quantitatively compared between the NR middle (blue) and end (red) positions and the summary bar graphs are presented for the two NRs discussed in Figures 4 and 5. The degree of chemical reactivity towards sulfidation was revealed to be higher at the end than the middle positions of the NRs. **(B)** Representative bar graph for 10 independent sulfidized NRs showing the Raman intensities measured from the middle (blue) versus the end (red) on the same NRs. The left panel contains the Raman intensities at 261 cm^{-1} measured under 532 nm incident light. The right panel charts the peak intensities at 349 cm^{-1} collected with 405 nm incident light. Regardless of the incident laser wavelength

used or the ZnS phonon mode analyzed, the overall NR reactivity towards sulfidation was determined to be higher on the end relative to the side facet. **(C)** The bar graphs show normalized and averaged Raman intensities corresponding to all three ZnS peaks (70 cm^{-1}, 261 cm^{-1}, 349 cm^{-1}) collected by using 532 nm light. The bar graph results were obtained by examining 20 independent NRs. Only the higher NR end of the two termini was used for the analysis in the left panel whereas, in the right panel, the mean value at the two NR termini was considered before normalizing the intensity values from each position against the end intensity. In all cases, the reactivity towards sulfidation was found to be higher on the end than the middle position of the NRs.

To better understand how the sulfidation reaction proceeds, we carried out subsequent Raman scattering measurements by directly tracking the same ZnO NRs before and after reaction with TAA. For these sets of NRs, positional Raman data were collected from both the middle and end locations of the pristine as well as S-reacted ZnO NRs for the same NRs with 405 nm excitation. We then analyzed the ZnS peak at 349 cm^{-1} and the SO mode centered at 334 cm^{-1}. Figures 7(A) and 7(B) display representative Raman spectra of ZnO NRs taken before and after the sulfidation reaction from the NR's middle and end positions. In each graph, the black spectrum represents the pristine ZnO NR signals at the given NR position. The blue and red spectra correspond to the data taken from the middle and end positions, respectively, of the same NR after sulfidation. In the 'before' spectrum showing the Raman frequency window of 280-460 cm^{-1} in Figures 7(A) and 7(B), the NR displayed ZnO phonon modes of E_{2H}-E_{2L}, E_{1T}, and E_{2H}. After sulfidation, the Raman spectra of the same NR yielded a broad peak spanning the region of 320-360 cm^{-1}. The inset in each figure represents a peak fitting of this broad feature whose overall intensity is contributed by two ZnS phonon modes, one at 334 cm^{-1} due to the SO mode and the other at 349 cm^{-1} corresponding to the A_{1L}/E_{1L} modes. The bar graphs in Figures 7(C) and 7(D) present the normalized intensities of the SO and A_{1L}/E_{1L} peaks of ZnS, respectively, obtained from 10 separate NRs

after performing position-resolved Raman investigations on the same NRs before and after TAA reaction. The outcomes in Figures 7(C) and 7(D) also show that the NR ends exhibit higher ZnS signal than the middle, suggesting that the NR end facets have a higher reactivity towards ZnS formation. Combined with the results discussed in Figure 6, the Raman scattering results in Figure 7 unambiguously show that the higher NR end reactivity relative to the middle is persistent regardless of the excitation wavelength, ZnS phonon peak, or the specific NR terminus analyzed.

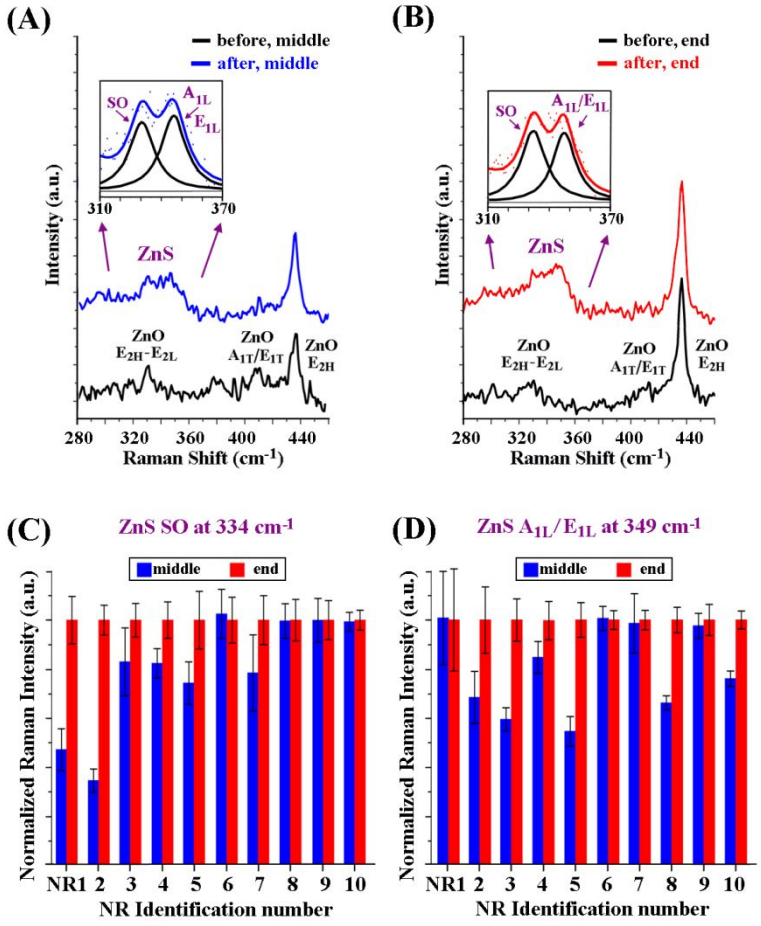

Figure 7. NR facet-specific S-reactivity further substantiated by tracking the same NRs before and after sulfidation with NR position-resolved Raman spectroscopy. The same ZnO NRs were examined before and after the reaction at the NR middle (blue) and end (red) locations under 405 nm illumination. **(A and**

B) The representative data sets show typical Raman spectra and associated peak fittings when tracking ZnO NRs before and after their reaction with TAA. The Raman data acquired from the middle and end positions of a ZnO NR are shown in (A) and (B), respectively. The insets display a peak fitting of the new Raman feature detected in the 320-360 cm^{-1} frequency region following sulfidation, which is attributed to the co-located SO and A_{1L}/E_{1L} modes of ZnS. **(C and D)** The bar graphs display the normalized intensities for the peak at (C) 334 cm^{-1} and (D) 349 cm^{-1} from 10 exemplar NRs by tracking their Raman scattering intensities from the NR middle (blue) and end (red) locations before and after sulfidation. For both phonon modes analyzed, the reactivity of the end facets on the NR is determined to be higher than the side facets towards sulfidation.

Summary

In summary, we have successfully demonstrated that position-resolved Raman spectroscopy can be used to reveal the different crystal facet-dependent reactivities associated with the sulfidation reaction of ZnO NRs at the single nanomaterial level. We have conclusively shown that the end (basal) facets of ZnO NRs are more prone to sulfidation than the middle (main body) facets by quantitatively comparing various S-induced phonon scattering intensities measured from different positions on the same ZnO NRs and by tracking the same NRs with Raman spectroscopy before and after sulfidation reaction. The sulfidation trends found from the NR facet-resolved Raman scattering results were further substantiated by the electron microscopy and fluorescence emission data taken on the same NRs. Such single crystal level insight on the facet-dependent sulfidation reactivity of ZnO NRs may furnish fundamentally guided, nanomaterial design principles beneficial to many technological and industrial applications exploiting the conversion of ZnO NRs to ZnS. Together with the wealth of knowledge in the literature for producing ZnO nanomaterials into a variety of crystal shapes and structures,[24,25,37,43] our endeavors in this work may be broadly applicable in developing more effective, low-dimensional, ZnO-based sorbents and scrubbers

for H_2S removal. More generally, the position-resolved Raman spectroscopy approach we demonstrate in this paper can be applied to quantify distinct, facet-dependent chemical reactivities of other technologically important nanomaterials. It can be also used to determine chemical reaction-triggered phonon modes from given nanomaterial crystal planes. Owing to the exquisite chemical sensitivity of Raman spectroscopy, the approach will be particularly beneficial for examining nanomaterials at the single crystalline facet level and at a low chemical reaction state whose weak chemical signals and reaction degrees may be difficult to quantify otherwise.

Conflicts of Interest Statement: There are no conflicts of interest to declare.

Acknowledgements

The authors acknowledge financial support of this work by the ACS Petroleum Research Fund Award (55283-ND10), the National Science Foundation (NSF) ENG CBET Award (CBET1841373), and the NSF Major Research Instrumentation Award (CHE1429079).

Footnote

†Electronic supplementary information (ESI) available: Additional EDX spectra and chemical elemental maps collected from a moderately sulfidized NR are presented in Figure S1.

References

1. X. Fang, T. Zhai, U. K. Gautam, L. Li, L. Wu, Y. Bando and D. Golberg, *Prog. Mater. Sci.*, 2011, **56**, 175-287.
2. X. Wang, P. Gao, J. Li, C. J. Summers and Z. L. Wang, *Adv. Mater.*, 2002, **14**, 1732-1735.
3. D. F. Moore, Y. Ding and Z. L. Wang, *J. Am. Chem. Soc.*, 2004, **126**, 14372-14373.
4. J. S. Hu, L. L. Ren, Y. G. Guo, H. P. Liang, A. M. Cao, L. J. Wan and C. L. Bai, *Angew. Chem. Int. Ed.*, 2005, **44**, 1269-1273.
5. A. T. Atimtay and D. P. Harrison, *Desulfurization of Hot Coal Gas*, Springer, New York, NY, 1998.
6. C. L. Carnes and K. J. Klabunde, *Chem. Mater.*, 2002, **14**, 1806-1811.
7. A. M. Karim, T. Conant and A. K. Datye, *Phys. Chem. Chem. Phys.* , 2008, **10**, 5584-5590.
8. X. Wang, T. Sun, J. Yang, L. Zhao and J. Jia, *Chem. Eng. J.*, 2008, **142**, 48-55.
9. P. R. Westmoreland, J. B. Gibson and D. P. Harrison, *Environ. Sci. Technol.*, 1977, **11**, 488-491.
10. B. Awume, M. Tajallipour, M. Nemati and B. Predicala, *Water Air Soil Pollut.*, 2017, **228**, 147.
11. A. C. Alvarado, B. Z. Predicala and D. A. Asis, *Int. J. Environ. Sci. Technol.*, 2014, **12**, 893-904.
12. H. B. Ahn and J. Y. Lee, *Cryst. Eng. Comm.*, 2013, **15**, 6709-6714.
13. M. Behl, J. Yeom, Q. Lineberry, P. K. Jain and M. A. Shannon, *Nat. Nanotechnol.*, 2012, **7**, 810-815.
14. L. Neveux, D. Chiche, J. Perez-Pellitero, L. Favergeon, A. S. Gay and M. Pijolat, *Phys. Chem. Chem. Phys.*, 2013, **15**, 1532-1545.
15. J. J. Uhlrich, R. Franking, R. J. Hamers and T. F. Kuech, *J. Phys. Chem. C*, 2009, **113**, 21147-21154.
16. C. Yan and D. Xue, *J. Phys. Chem. B*, 2006, **110**, 25850-25855.
17. R. Ma, C. Levard, F. M. Michel, G. E. Brown and G. V. Lowry, *Environ. Sci. Technol.*, 2013, **47**, 2527-2534.

18. R. Portela, F. Rubio-Marcos, P. Leret, J. F. Fernández, M. A. Bañares and P. Ávila, *J. Mater. Chem. A*, 2015, **3**, 1306-1316.

19. E. Sasaoka, S. Hirano, S. Kasaoka and Y. Sakata, *Energy Fuels*, 1994, **8**, 1100-1105.

20. T. A. Saleh, *Applying Nanotechnology to the Desulfurization Process in Petroleum Engineering*, Engineering Science and Reference, Hershey, PA, 2015.

21. M. S. Morgani, R. Saboori and S. Sabbaghi, *Mater. Res. Express*, 2017, **4**, 075501.

22. X. M. Shuai and W. Z. Shen, *J. Phys. Chem. C*, 2011, **115**, 6415-6422.

23. H. J. Fan, U. Gösele and M. Zacharias, *Small*, 2007, **3**, 1660-1671.

24. Z. L. Wang, *J. Phys.: Condens. Matter*, 2004, **16**, R829-858.

25. Z. L. Wang, *ACS Nano*, 2008, **2**, 1987-1992.

26. P. Yang, H. Yan, S. Mao, R. Russo, J. Johnson, R. Saykally, N. Morris, J. Pham, R. He and H. J. Choi, *Adv. Funct. Mater.*, 2002, **12**, 323-331.

27. J. Hahm, *J. Nanosci. Nanotech.*, 2014, **14**, 475-486.

28. J. Hahm, *Ann. Rev. Phys. Chem.*, 2016, **67**, 691-717.

29. C. A. Arguello, D. L. Rousseau and S. P. S. Porto, *Phys. Rev.*, 1969, **181**, 1351-1363.

30. J. M. Calleja and M. Cardona, *Phys. Rev. B*, 1977, **16**, 3753-3761.

31. J. Serrano, A. Cantarero, M. Cardona, N. Garro, R. Lauck, R. E. Tallman, T. M. Ritter and B. A. Weinstein, *Phys. Rev. B*, 2004, **69**.

32. J. Trajić, R. Kostić, N. Romčević, M. Romčević, M. Mitrić, V. Lazović, P. Balaž and D. Stojanović, *J. Alloys Compd.*, 2015, **637**, 401-406.

33. J. Díaz-Reyes, R. S. Castillo-Ojeda, R. Sánchez-Espíndola, M. Galván-Arellano and O. Zaca-Morán, *Curr. Appl. Phys.*, 2015, **15**, 103-109.

34. Y. C. Cheng, C. Q. Jin, F. Gao, X. L. Wu, W. Zhong, S. H. Li and P. K. Chu, *J. Appl. Phys.*, 2009, **106**, 123505.

35. Q. Xiong, J. Wang, O. Reese, L. C. Lew Yan Voon and P. C. Eklund, *Nano Lett.*, 2004, **4**, 1991-1996.

36. M. Singh, S. Song and J. Hahm, *Nanoscale*, 2014, **6**, 308-315.

37. Ü. Özgür, Y. I. Alivov, C. Liu, A. Teke, M. A. Reshchikov, S. Doğan, V. Avrutin, S.-J. Cho and H. Morkoç, *J. Appl. Phys.*, 2005, **98**, 041301.

38. J. Smith, A. Akbari-Sharbaf, M. J. Ward, M. W. Murphy, G. Fanchini and T. K. Sham, *J. Appl. Phys.*, 2013, **113**, 093104.

39. Z. G. Wang, X. T. Zu, S. Zhu and L. M. Wang, *Physica E*, 2006, **35**, 199-202.

40. H. Hiroshi, *J. Phys. Condens. Matter*, 2002, **14**, R967.

41. M. Hansen, J. Truong, T. Xie and J.-i. Hahm, *Nanoscale*, 2017, **9**, 8470-8480.

42. J. Hüpkes, J. I. Owen, S. E. Pust and E. Bunte *Chem. Phys. Chem.*, 2012, **13**, 66-73.

43. L. E. Greene, B. D. Yuhas, M. Law, D. Zitoun and P. Yang, *Inorg. Chem.*, 2006, **45**, 7535-7543.

TOC Graphics